Optical Engineering

SPIEDigitalLibrary.org/oe

Passive millimeter-wave imaging with compressive sensing

Nachappa Gopalsami
Shaolin Liao
Thomas W. Elmer
Eugene R. Koehl
Alexander Heifetz
Apostolos C. Raptis
Leonidas Spinoulas
Aggelos K. Katsaggelos

SPIE

Passive millimeter-wave imaging with compressive sensing

Nachappa Gopalsami
Shaolin Liao
Thomas W. Elmer
Eugene R. Koehl
Alexander Heifetz
Apostolos C. Raptis
Nuclear Engineering Division
Argonne National Laboratory
Lemont, Illinois 60439
E-mail: gopalsami@anl.gov

Leonidas Spinoulas
Aggelos K. Katsaggelos
Northwestern University
Department of Electrical Engineering and Computer Science
Evanston, Illinois 60208

Abstract. Passive millimeter-wave (PMMW) imagers using a single radiometer, called single pixel imagers, employ raster scanning to produce images. A serious drawback of such a single pixel imaging system is the long acquisition time needed to produce a high-fidelity image, arising from two factors: (a) the time to scan the whole scene pixel by pixel and (b) the integration time for each pixel to achieve adequate signal to noise ratio. Recently, compressive sensing (CS) has been developed for single-pixel optical cameras to significantly reduce the imaging time and at the same time produce high-fidelity images by exploiting the sparsity of the data in some transform domain. While the efficacy of CS has been established for single-pixel optical systems, its application to PMMW imaging is not straightforward due to its (a) longer wavelength by three to four orders of magnitude that suffers high diffraction losses at finite size spatial waveform modulators and (b) weaker radiation intensity, for example, by eight orders of magnitude less than that of infrared. We present the development and implementation of a CS technique for PMMW imagers and shows a factor-of-ten increase in imaging speed. [DOI: 10.1117/1.OE.51.9.091614]

Subject terms: millimeter waves; passive imaging; compressive sensing; Hadamard masks.

Paper 120207SSP received Feb. 14, 2012; revised manuscript received Jun. 27, 2012; accepted for publication Aug. 14, 2012; published online Sep. 14, 2012.

1 Introduction

Passive millimeter wave (PMMW) imaging has many applications, such as remote sensing of the Earth's resources, aircraft landing in optically obscure weather, and security point inspection of concealed weapons in humans.[1] The Earth's resources that may be sensed by passive MMWs include terrain mapping, soil moisture and polar ice mapping, ocean surface sensing, as well as atmospheric water vapor and temperature profiling as a function of altitude for climate modeling and weather sensing.[2] The underlying principle is the measurement of Planck's blackbody radiation of materials at millimeter wavelengths. The main advantage of passive MMW imaging is that it provides information about ground-based targets under all weather conditions; optical systems [visible and infrared (IR)], on the other hand, require clear atmospheric conditions for reliable operation. For example, the atmospheric attenuation of MMW frequencies at sea level is 0.07 to 3 dB/km in drizzle and fog, whereas it is one to three orders of magnitude higher for optical frequencies (exceeding 100 dB/km in foggy conditions).[3–5] Excellent image contrast is obtained in outdoor environments due to cold sky-reflected radiation by targets. For example, the apparent temperature of the sky in clear weather at 94 GHz is 70 K in comparison to 220 K at infrared wavelengths. Even at the same ambient temperature, there exists variation in MMW thermal contrast of objects because of their emissivity differences at these wavelengths, e.g., the emissivity[6] of metal is ≈0, water 0.4, wood 0.4, and concrete 0.8. Signal "washouts" do not occur since the apparent temperature between the background and the object is rarely the same.

In addition to imaging, passive MMWs can be used to obtain spectroscopic signatures of chemicals based on molecular rotational energy transitions.[7] With a 16-channel filter bank in the 146 to 154 GHz band, we have measured the 150 GHz spectral line of nitric oxide from a test stack at a distance of 600 m from the radiometer.[8] We upgraded the MMW spectrometer into an integrated imaging and spectroscopy system for broad area search and detection of nuclear facilities.[9,10] Figure 1 is an example of an outdoor image of a dome-shaped building at 300 m, in which the passive MMW image is overlaid on optical image using augmented reality technique.

A major disadvantage of such a single-pixel imaging system is the long scanning time that it takes for image acquisition. For example, the 100×100 pixel image of Fig. 1 with 1 s integration time per pixel took about 3 h. Such a long imaging time diminishes the imager's value for applications involving nonstationary objects. We have investigated the application of compressive sensing (CS) techniques in this paper as they have the potential to reduce the image acquisition time by a factor of 10 or more.

2 Compressive Sensing with Coded Aperture Masks

CS involves exploiting the sparsity or compressibility of an image in some transform domain such that one can utilize fewer measurements (fewer samples) than the ones required for conventional imaging, yet the image can be reconstructed with minimal loss of information. While conventional data compression techniques, such as JPEG, use bandwidth

0091-3286/2012/$25.00 © 2012 SPIE

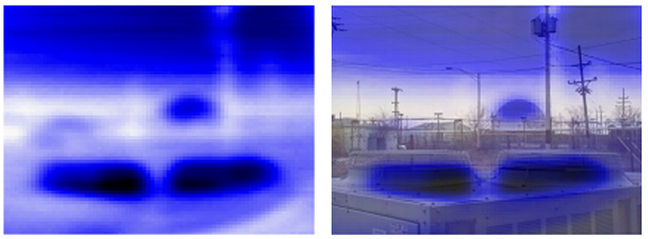

(a) (b)

Fig. 1 Passive MMW image (a) of an outdoor scene overlaid on optical image (b); the scene consists of a dome-shaped building at 300 m from the imager.

compression for efficient storage and communication purposes after a full image is collected, CS techniques exploit compression in signal/image structure and collect fewer data, thus saving on imaging time.[11]

In order to guarantee lossless image reconstruction by CS theory, the acquisition matrix must satisfy the restricted isometry property (RIP).[12–14] Matrices that are known to satisfy the RIP condition with high probability include matrix elements drawn from Gaussian independent and identically distributed (iid) random numbers.[14] Because iid-based spatial light modulation is difficult to implement, binary representation of the iid random numbers is used in practice. Digital micromirror devices (DMD) have been used in single-pixel optical cameras in which random masks are created by electronically orienting them into one of two reflecting positions.

Unlike DMDs that are individually controlled to reflect the incident light beam toward (on) or away (off) from the imaging lens, one may use coded apertures with binary elements representing transmission (on) or reflection (off) of the light. Feasibility of CS with such masks was tested in an active MMW system by inserting a sequence of prefabricated printed circuit masks in a collimated MMW beam and collecting mask-modulated radiation through a dielectric object to be imaged.[15] The manual introduction of masks as above defeats the purpose of fast imaging by CS. In this paper, we present for the first time a novel method of implementing CS in passive MMW imagers. Compared to active MMWs, passive MMW radiation is very weak and incoherent; as a result, the quasioptical components in passive MMW systems must be carefully designed to minimize diffraction losses by the masks and maximize the signal-to-noise ratio (SNR).

We used Hadamard transform masks as coded apertures for light modulation as they offer a practical means of introducing random selection of Hadamard patterns using a single extended mask. Like random binary numbers, randomized Hadamard patterns, such as the scrambled block Hadamard ensemble, are also known to satisfy the RIP property.[16] While our imaging setup, in principle, can employ scrambled block Hadamard ensemble, we followed a slight variation of it in that the Hadamard patterns were chosen from a random selection of the rows of a cyclic S-matrix derived from the Hadamard transform theory.[17] The main advantage is that the reconstruction problem becomes linear in the form of simple matrix manipulation of the S-matrix, significantly reducing the computation burden and time involved with the nonlinear minimization reconstruction algorithms used in traditional CS methods.

2.1 *Design and Fabrication of Hadamard Masks*

Instead of using M random masks one at a time, a single extended Hadamard mask, H_e, may be constructed that encompasses all possible Hadamard patterns as submatrices. The procedure to construct an extended Hadamard mask is as follows. A cyclic S-matrix of size $pq \times pq$, where p and q are prime numbers and $q = p + 2$, is formed using the twin prime construction method by which a row of pq elements of value 0 or 1 is produced by a set of rules on the i'th element based on the remainders of i/p and i/q.[17] Once the first row of S is formed, the S-matrix can be completed by shifting the row by one element to the left and filling the missing rightmost element in a circular pattern. Taking $p = 5$ and $q = 7$ as an example, Fig. 2(a) gives the S-matrix in which black represents 0 and white 1. To form the extended Hadamard mask, the elements of the first row of the S-matrix are folded into a $p \times q$ matrix that is concatenated to the right and below to form a $(2p-1) \times (2q-1)$ matrix as shown in Fig. 2(b). From the extended Hadamard mask, one can randomly choose pq Hadamard acquisition matrices H_i, $i = 1$ to pq by matching the top left corner of a template of size $p \times q$ to the location (k, l) in H_e, where $i = (k-l)q + l$ corresponds to the i'th row of the S-matrix.

The design of mask size and pixel resolution is based on the following considerations:

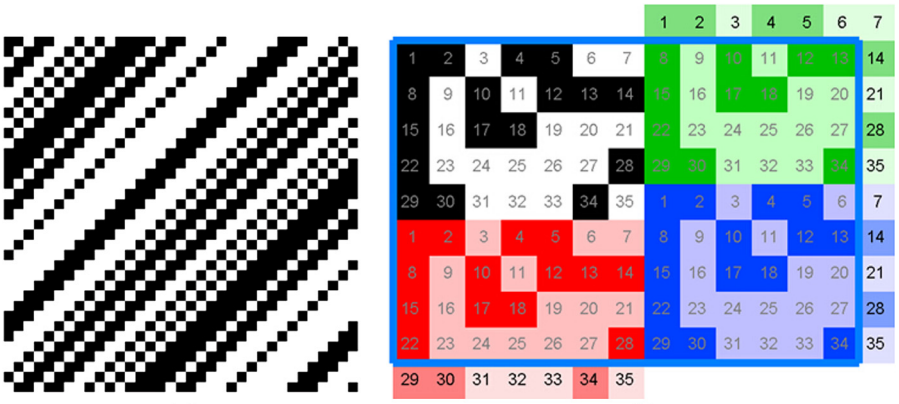

(a) (b)

Fig. 2 The elements of cyclic S matrix (a) and extended Hadamard matrix H_e shown by the box (b) for $p = 5$ and $q = 7$. The dark shades represent 0 and the light shades 1. The matrix elements are indentified by numbers 1 to 35 in (b).

- Pixel size, s is such that $s > \lambda/2$ to reduce diffraction losses by subwavelength size holes (where $\lambda = 2$ mm is the wavelength of millimeter waves at 150 GHz)
- Mask size, $ps \times qs$, should match the MMW image plane at the mask location
- Image pixels $>40 \times 40$ for adequate image resolution
- p and q with $q = p + 2$ must be prime numbers for cyclic $\boldsymbol{S}$ matrix generation

We used $p = 41$ and $q = 43$ with a pixel size of 1.24 mm and produced an extended cyclic mask of 81×85 pixels of size 10.04×10.53 cm. Each $p \times q$ mask is of size 50.84×53.32 mm. The extended Hadamard mask was fabricated using chrome coating on a millimeter-wave transparent quartz plate, as shown in Fig. 3. The colored boxes show two of the 1763 possible Hadamard patterns that can be created by exposing parts of the mask.

3 Compressive Sensing Passive MMW Imager

3.1 *Imager Setup*

Figure 4 shows a two-lens passive millimeter-wave setup for CS implementation using Hadamard masks. The extended Hadamard mask is placed at the image plane of a six-in. lens, where the image of a distant target is formed. A metal plate (template) with a hole of size $p \times q$ is placed in front of the mask, which defines the exposure window. The extended mask is controlled by a two-axis translation stage to expose different mask patterns for compressive data collection, one for each measurement. A second lens of 1-inch diameter collects the modulated radiation field through the Hadamard mask and focuses it onto the multichannel radiometer. The positions of the lenses and the mask are governed by the lens equation: $1/f_r = 1/d_i + 1/d_o$, where f_r is the focal length of either of the lenses, and d_i and d_o are the image and object distances, respectively. Because the targets used in these experiments do not have spectral features, we averaged all 16 spectral channels, which offers an increase of SNR by a factor of four.

Fig. 3 An extended Hadamard mask of size 81×85 pixel fabricated on a quartz plate with chrome coating. A 41×43 pixel mask area such as the ones indicated by the colored boxes is exposed for each acquisition.

3.2 *SNR Analysis of CS Imager Setup*

It is important to compare the SNR between the raster scanning and CS systems to ensure that the reduction in imaging time obtained with the latter does not come at the expense of the radiometer sensitivity. A reduction in sensitivity by a factor x in the CS setup is equivalent to a reduction in the integration time by a factor of $1/x^2$ in the raster scanning setup, as the sensitivity of a Dicke-switched radiometer is given by: $\Delta T = 2T_N/\sqrt{B\tau}$, where T_N is the noise temperature of the receiver, B is the predetection bandwidth, and τ is the postdetection integration time. For example, if the CS setup offers a reduction in imaging time by a factor of 10 at a cost of 3.16 times less in sensitivity ($3.16\Delta T$), the same saving in imaging time can be obtained with conventional imaging by reducing the integration time by ten times for an equivalent sensitivity of $3.3\Delta T$. However, if the raster scanning system uses a stop-and-go implementation for data collection at each pixel, the total acquisition time including the translation time of the raster scanning system can be substantially longer than that of the CS system.

Figure 5 shows ray tracing diagrams of raster-scanned and CS-based signal acquisitions. While the raster scanning system collects the radiation from each pixel of the target, the CS system in principle sums up the radiation from $\sim N/2$ pixels (as approximately half of the pixels in the mask are open) of the target. If there were to be no loss due to the mask or in the radiation collection from the target to the radiometer, the SNR of the CS system would be $\sqrt{N/2}$ times the raster scanned system as the noise is averaged while the signal related to the target temperature remains the same. In practice, however, radiation losses occur due to (a) diffraction effects from the subwavelength-sized mask

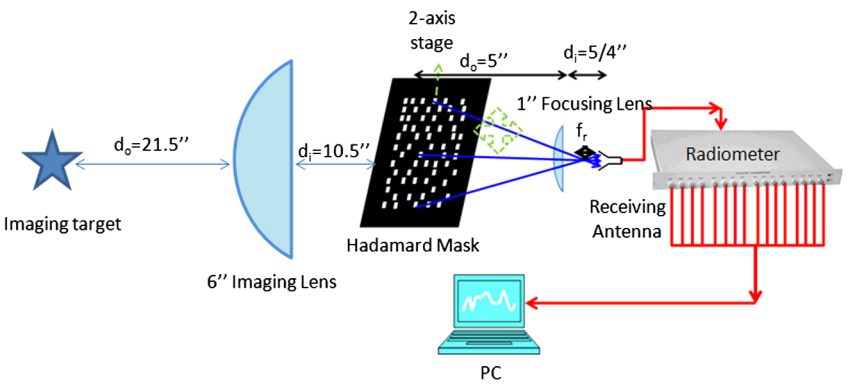

Fig. 4 Compressive sensing setup for passive MMW imaging.

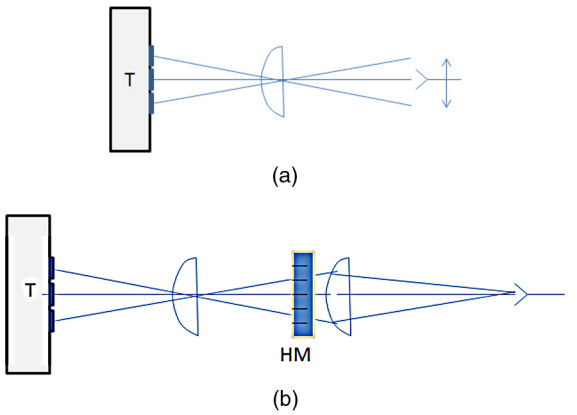

Fig. 5 Signal acquisition by (a) raster scanned camera and (b) CS-based single-pixel camera.

apertures and (b) inefficient radiation collection by the finite-size lenses. The diffraction loss due to the mask may be analyzed as follows. Each aperture in the mask can be treated as a dipole antenna[18] radiating over a spherical area and only part of this radiation is collected by the 1-in. diameter lens. The actual intensity of each pixel collected by the radiometer can be expressed as: $\tilde{I}_{\text{pixel}} = wI_{\text{pixel}}$, where I_{pixel} is the intensity of a single pixel, and w is the fraction of the intensity collected by the radiometer. For the experimental setup in Fig. 4, w is the ratio of the area of the focusing lens and that of the spherical surface at a distance d_o. Accordingly, $w = A_{\text{lens}}/4\pi d_o^2 = 4\pi r_{\text{lens}}^2/4\pi d_o^2 = (r_{\text{lens}}/d_o)^2$. For $r_{\text{lens}} = 1.27$ cm and $d_o = 12.7$ cm, $w = (r_{\text{lens}}/d_o)^2 \approx 1\%$ and $\tilde{I}_{\text{pixel}} = wI_{\text{pixel}} \approx 1\% \times I_{\text{pixel}}$. The total intensity from all pixels collected by the radiometer is thus given by $\tilde{I} = 0.5wpq\tilde{I}_{\text{pixel}} \approx 0.5\% \times p(p+2) \times I_{\text{pixel}}$, where we have assumed uniform intensity from all the pixels. For $p = 41$, we get $\tilde{I} \approx 0.5\% \times p(p+2) \times I_{\text{pixel}} \approx 9I_{\text{pixel}}$. Hence, the corresponding improvement in SNR is estimated as three times that of the raster scanned imagers. The two-lens setup we have used is not an optimal design for radiation collection since a large portion of the radiation from the target does not reach the radiometer. With better collection efficiency and higher pixel count N, the SNR of the CS system is expected to be higher than that of the raster-scanned setup. Furthermore, there is a tradeoff between pixel size (image resolution) and SNR; with a larger aperture (lower resolution), the diffraction losses will be less, resulting in a higher w and, in turn, a higher SNR.

4 Image Reconstruction

4.1 *Image Reconstruction from Full Hadamard Acquisitions*

If a complete set of N acquisitions is obtained by fully raster scanning the extended Hadamard mask, the image reconstruction consists of simple matrix manipulations as given below. The measured intensity vector $\boldsymbol{I}_m$ using Hadamard masks may be expressed as[19]

$$\boldsymbol{I}_m = \boldsymbol{S} \cdot \boldsymbol{I}_s, \tag{1}$$

where $\boldsymbol{S}(pq\,x\,pq)$ is the cyclic $\boldsymbol{S}$-matrix realized by the Hadamard mask and $\boldsymbol{I}_s(pq \times 1)$ is the scene intensity vector, which can be reconstructed from the full set of Hadamard measurements by

$$\boldsymbol{I}_s - \boldsymbol{S}^{-1}\boldsymbol{I}_m. \tag{2}$$

For a given Hadamard mask size, the $\boldsymbol{S}$ matrix in Eq. (2) can be predetermined from the Hadamard sequence, so the image reconstruction is very fast.

To test image formation and reconstruction, we used a single lens imaging setup as in Fig. 6, with a light bulb (thermal light source) illuminating an object and the Hadamard mask placed behind the object in close proximity. The relative sizes of the object (at the mask) and images for the single-lens setup may be determined using the ray tracing diagram in Fig. 6. According to the lens equation, the object and image distances d_0 and d_i are given by $1/d_o + 1/d_i = 1/f$, where f is the focal length. With $d_o = 12.7$ cm and $f = 2.54$ cm, $d_i = 3.175$ cm. The magnification is given by $M \equiv b/a = d_i/d_o = 1/4$, where b and a are the object and image sizes, respectively. For an antenna of radius $r_{\text{antenna}} = 0.3175$ cm, the field of view (FOV) is $\text{FOV} \equiv 2a = 2b/M = 2r_{\text{antenna}}/M = 8r_{\text{antenna}} = 2.54$ cm. The imaging setup we used provides only 2.54 cm FOV; as a result, we covered the imaging area for this setup with a metal plate having a 2.54 cm diameter hole. In order to expand the FOV to the full extent so that it covers the size of the Hadamard template (50.84×53.32 mm), the distances d_0 and d_1 may be changed to 22.86 and 2.8575 cm, respectively, keeping the lens diameter the same.

We first simulated the Hadamard transform and image reconstruction process for an object geometry consisting of a metal plate with a circular hole of diameter 2.54 cm and a 3-mm wide rectangular metal strip across the middle. Figure 7(a) gives the binary coded image of the object with 1 representing the hole and 0 the metal portion, and Fig. 7(b) is its Hadamard transformed image according to Eq. (1) after folding the $pq \times 1$ vector into a $p \times q$ matrix. The reconstructed image from Hadamard transformed data using Eq. (2) was exact and identical to Fig. 8(a) as there was no measurement noise for this ideal case.

We next obtained a full set of $pq = 1763$ Hadamard acquisitions by raster scanning the Hadamard mask. Figure 8(a) gives the Hadamard transformed image, and Fig. 8(b) shows the reconstructed image using Eq. (2). An excellent agreement is seen between the simulated [Fig. 7(b)] and experimental [Fig. 8(a)] Hadamard transformed images.

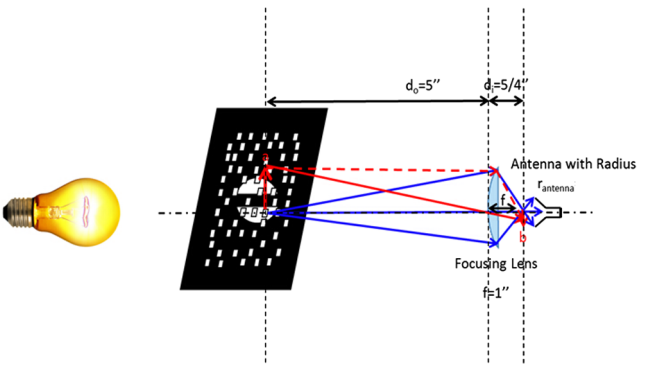

Fig. 6 Proof-of-principle test with a thermal light source illuminating an object consisting of a 2.54 cm diameter circular hole with a 3-mm wide rectangular metal strip.

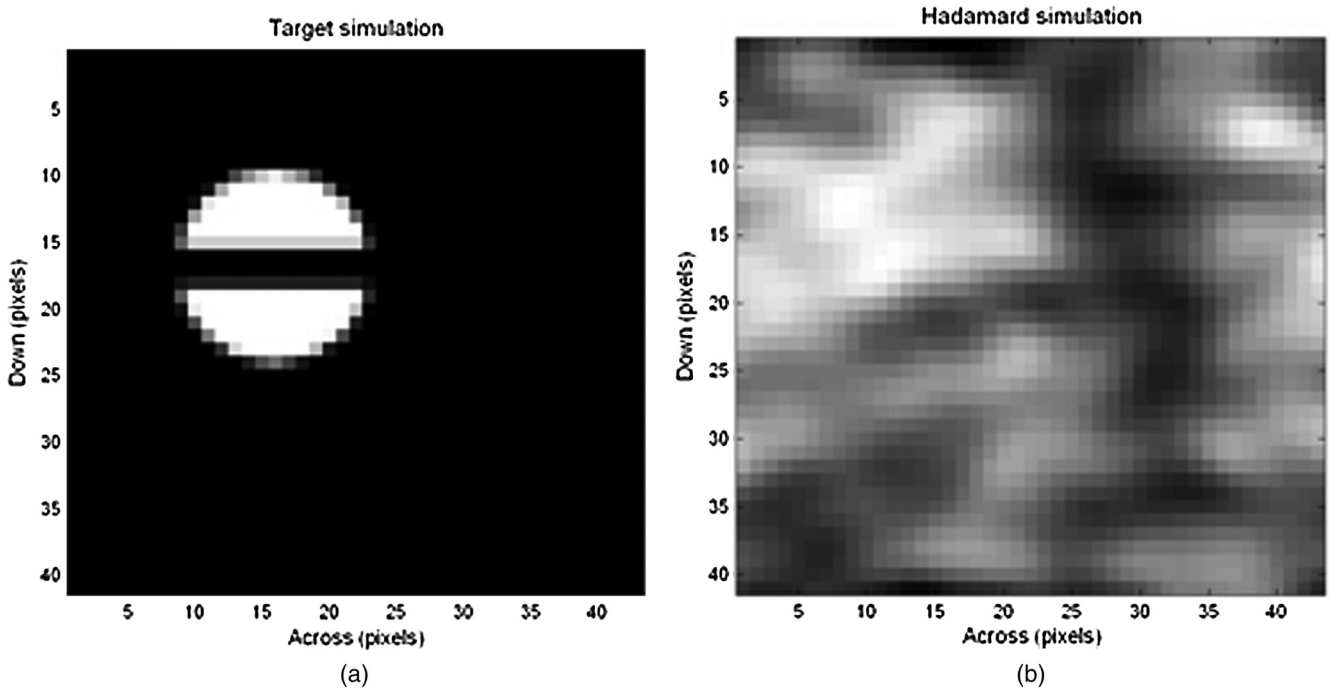

Fig. 7 Simulation of target geometry: (a) digitized image of circular hole with a strip in the middle and (b) simulated Hadamard transformed image.

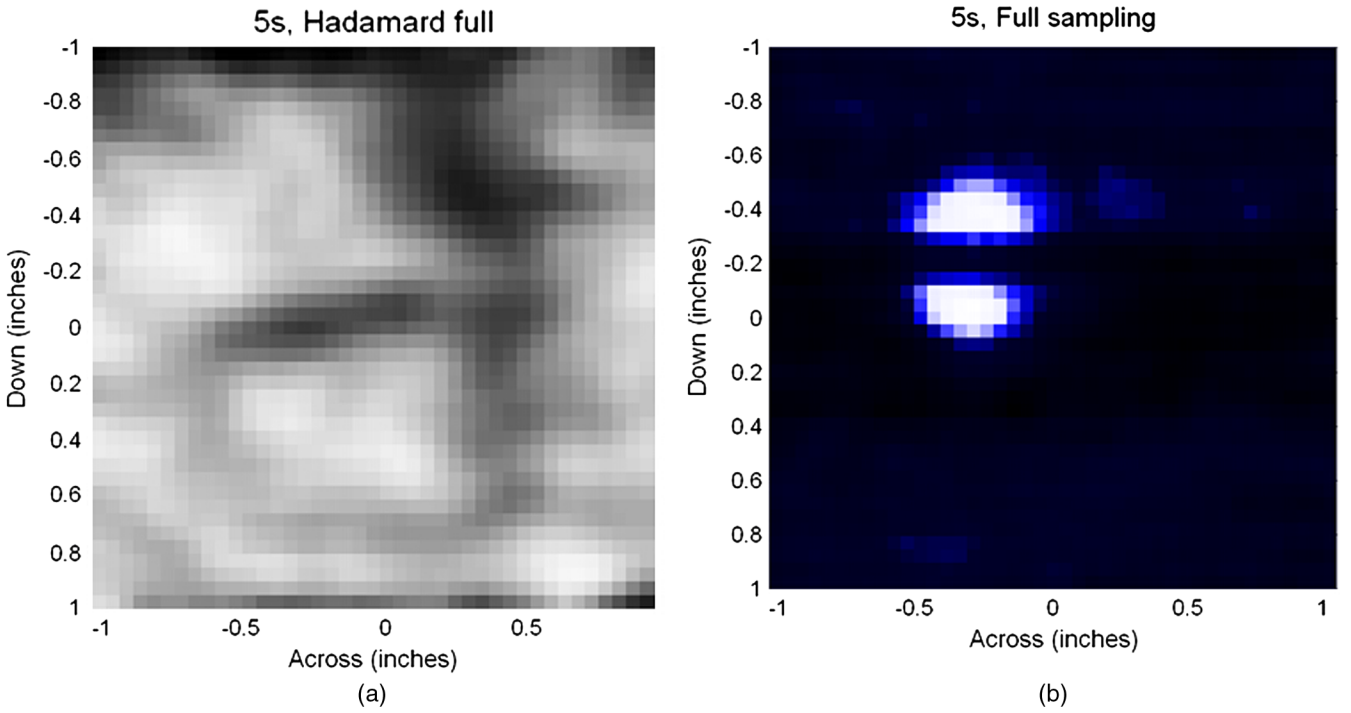

Fig. 8 Experimental data: (a) Hadamard-transformed image and (b) reconstructed image.

The reconstructed image of a circular hole with a horizontal metal strip shows the feasibility of Hadamard imaging at millimeter wavelengths with subwavelength resolution (1.24 mm pixel size for 2 mm wavelength).

4.2 *Image Reconstruction from Partial Hadamard Acquisitions*

Instead of fully scanning the extended Hadamard mask, one may sample the mask randomly or sequentially every n'th pixel in the horizontal and vertical directions. Figure 9 gives a flowchart of data acquisition and image reconstruction steps as the data acquisition proceeds. The measured data with the Hadamard matrices are in the Hadamard transform space. If the Hadamard transform space is complete with all pq acquisitions, the reconstruction is simply multiplication of the S^{-1} matrix with the unwrapped Hadamard transform data as presented before. To reconstruct from an incomplete data set in the Hadamard transform space (compressive

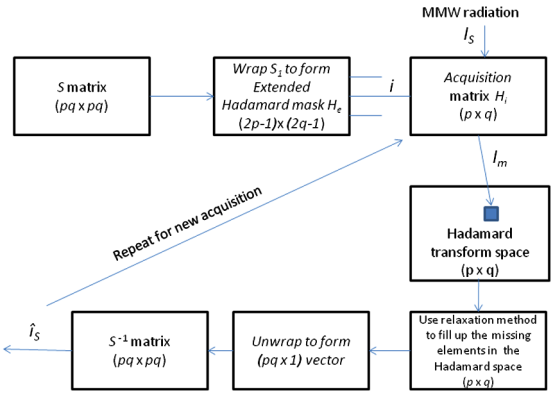

Fig. 9 Flowchart of Hadamard matrix acquisition and image reconstruction from compressively sampled data.

sampling), we introduce an iterative method of estimating the missing elements in the Hadamard transform space: the relaxation method, used in the numerical electrodynamics field.[20]

The relaxation method is based on iteratively estimating the two-dimensional (2-D) functional value $\langle\langle F(x,y)\rangle\rangle$ at the coordinate (x,y) from the nearest neighbors (straight) and next nearest neighbors (cross),

$$\langle\langle F(x,y)\rangle\rangle \equiv \frac{4}{5}\langle F(x,y)\rangle_S + \frac{1}{5}\langle F(x,y)\rangle_C,$$

where

$$\langle F(x,y)\rangle_S = \frac{1}{4}[F(x+h,y) + F(x,y+h) + F(x-h,y) + F(x,y-h)]$$

$$\langle F(x,y)\rangle_C = \frac{1}{4}[F(x+h,y+h) + F(x-h,y+h) + F(x+h,y-h) + F(x-h,y-h)]$$

and h is the distance between the grid points.

$$\begin{matrix}(x-h,y+h) & (x,y+h) & (x+h,y+h)\\ (x-h,y) & (x,y) & (x+h,y)\\ (x-h,y-h) & (x,y-h) & (x+h,y-h)\end{matrix}.$$

This is equivalent to applying a filter B at the grid (x,y):

$$B = \begin{pmatrix}1 & 4 & 1\\ 4 & 0 & 4\\ 1 & 4 & 1\end{pmatrix} \times \frac{1}{5\times 4}.$$

The iterative procedure consists of: 1. Enter the known values, 2. guess the missing elements, 3. apply the filter B and estimate the average value for (x,y), 4. reassert the known values and iterate on step 3 until desired convergence is reached. If the function is well behaved, convergence can be shown by a Taylor series analysis.[20]

To test the relaxation technique, we sampled every third column and third row of the Hadamard space, providing 1/9 of the full acquisitions. Figure 10(a) gives the recovered image in the Hadamard space, and Fig. 10(b) shows the reconstructed image of the object. The recovered Hadamard transformed image [Fig. 10(a)] from partial data compares well with the full Hadamard transformed image in Fig. 8(a). The reconstructed image of the object clearly shows the circular hole with a strip in the middle; however, the geometry looks somewhat distorted around sharp edges, which gets improved with additional samples.

4.3 *Progressive Compressive Sensing and Real-Time Image Reconstruction*

We developed a progressive sampling and image reconstruction method in which the Hadamard acquisition starts at every n'th row and n'th column in the Hadamard space. The relaxation technique is applied to fill the Hadamard space from which the image is reconstructed after every

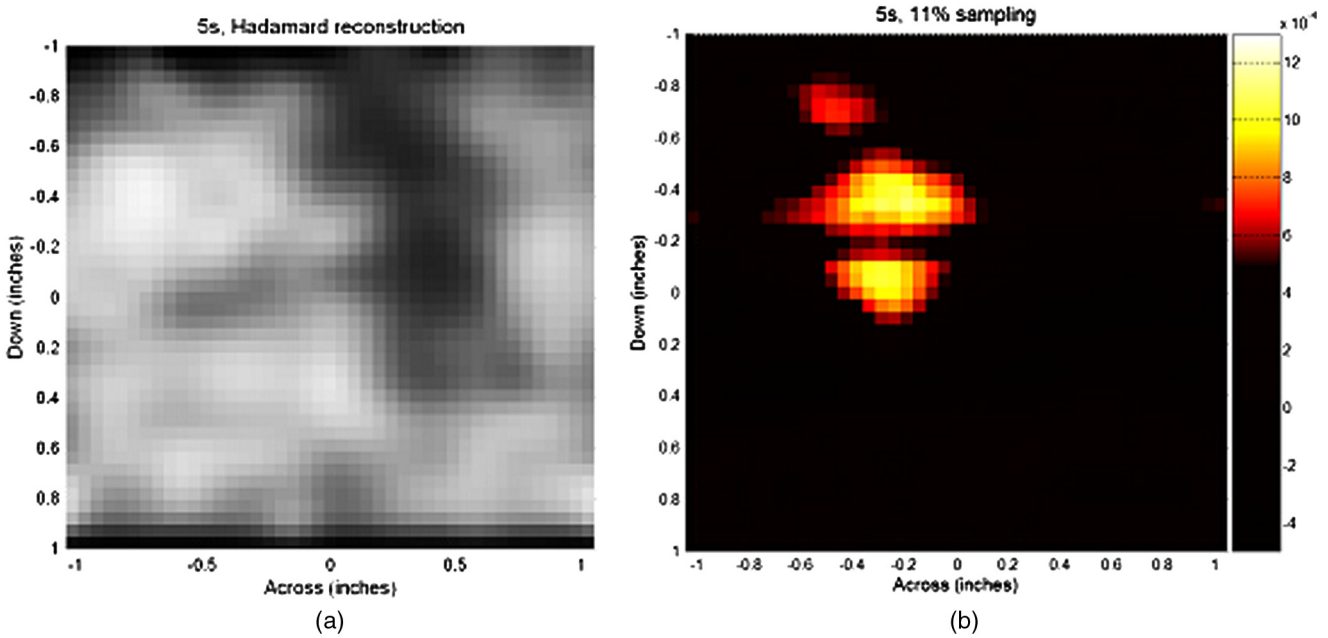

Fig. 10 Reconstructed image from 1/9th of samples: (a) relaxation method-based reconstruction of Hadamard space and (b) reconstructed image.

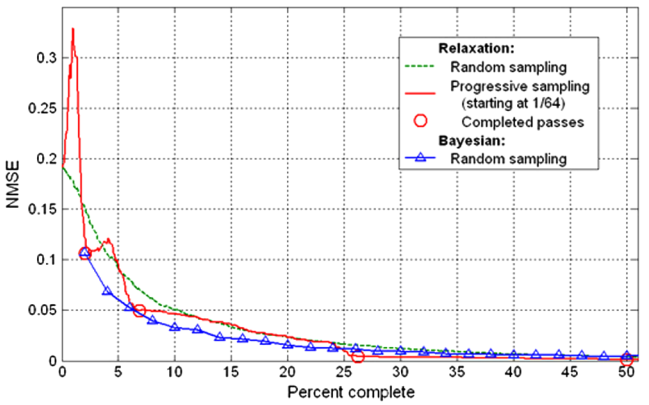

Fig. 11 Comparison of normalized mean square error (MSE) for progressive sampling and conventional random sampling methods.

sample in real time by Eq. (2), since the S-matrix is predetermined for a given p and q. If the image is not satisfactory, we continue sampling the Hadamard space in between the sampled points and reconstruct with $(2N/n)$ data, and so on. The sample space is progressively increased until satisfactory image quality is obtained. The complete image acquisition and reconstruction software is implemented in LabVIEW.

The reconstructed image quality using the progressive sampling method was compared against the Bayesian random sampling method that we had developed in the past.[21] A normalized mean squared error (NMSE) metric was adopted for comparison of reconstructed images from partial and full sets of samples. NMSE $= \Sigma_{i=1}^{N}(I_p(i) - I_f(i))^2 / \Sigma_{i=1}^{N}(I_f(i))^2$, where $I_p(i)$ and $I_f(i)$ are the intensities of the i'th pixel corresponding to the reconstructed images from partial and full acquisitions, respectively.

Figure 11 provides the comparison of NMSE versus the percent completion of the full acquisitions for the case of (a) relaxation method with random Hadamard patterns, (b) progressive sampling after each acquisition starting at 1/64 of full samples, (c) progressive sampling after each complete cycle in the Hadamard space, and (d) Bayesian reconstruction from random Hadamard acquisitions. The reconstructed image obtained after every complete cycle (e.g., $1/32, 1/16, \ldots, 1$) showed comparable or better performance than the random sampling methods. In addition, the computational time of the Hadamard transform-based reconstruction is significantly less than that of the conventional nonlinear minimization algorithms used in traditional CS reconstruction methods.

4.4 *Imaging with Two-Lens Setup*

The single lens imager setup shown in Fig. 6 was used for proof-of-principle testing of compressive sensing. To extend it to a full imaging system, we used a two-lens CS setup as shown in Fig. 4. To ensure high thermal contrast under indoors, a 60 W incandescent lamp (thermal source) was used as the target to be imaged. In outdoor conditions, however, such an artificial hot source is not needed as the cold sky reflected radiation would offer excellent thermal contrast. Figure 12 gives the reconstructed image of the lamp with (a) full and (b) 11% samples, and Fig. 13 gives that with one quarter of the lamp blocked by a metal plate with (a) full and (b) 11% samples. The reconstructed images with 11% samples compare well with those from full samples; however, there is a slight distortion in the object geometry due to the smoothing nature of the algorithm around sharp edges.

5 Conclusions

We have developed a CS approach for single-pixel passive millimeter wave imaging; it offers the potential to reduce the image acquisition time by a factor of 10 or more, obtain subwavelength pixel resolution, and achieve better SNR than with raster scanned systems. It is based on Hadamard transform masks for spatial intensity modulation, which allows for near real-time image reconstruction from partial samples. The traditional CS methods use acquisition matrices that satisfy the RIP or incoherence property that guarantees

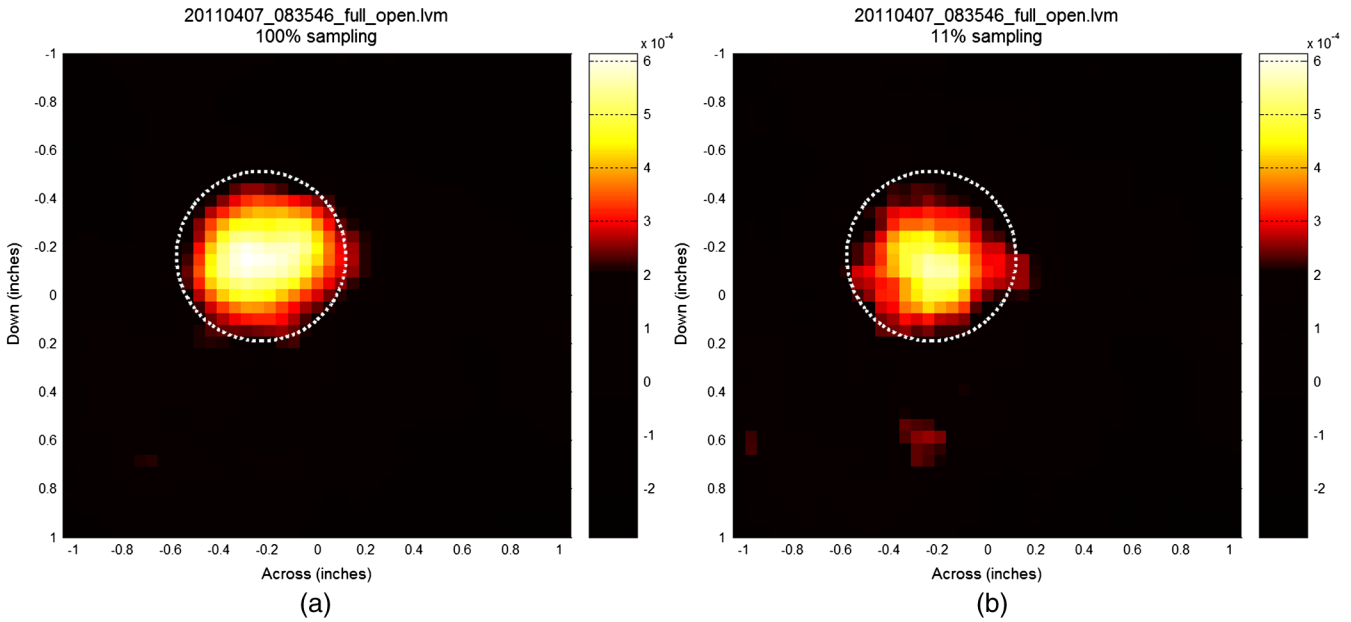

Fig. 12 Reconstructed image of lamp with (a) full and (b) 11% samples.

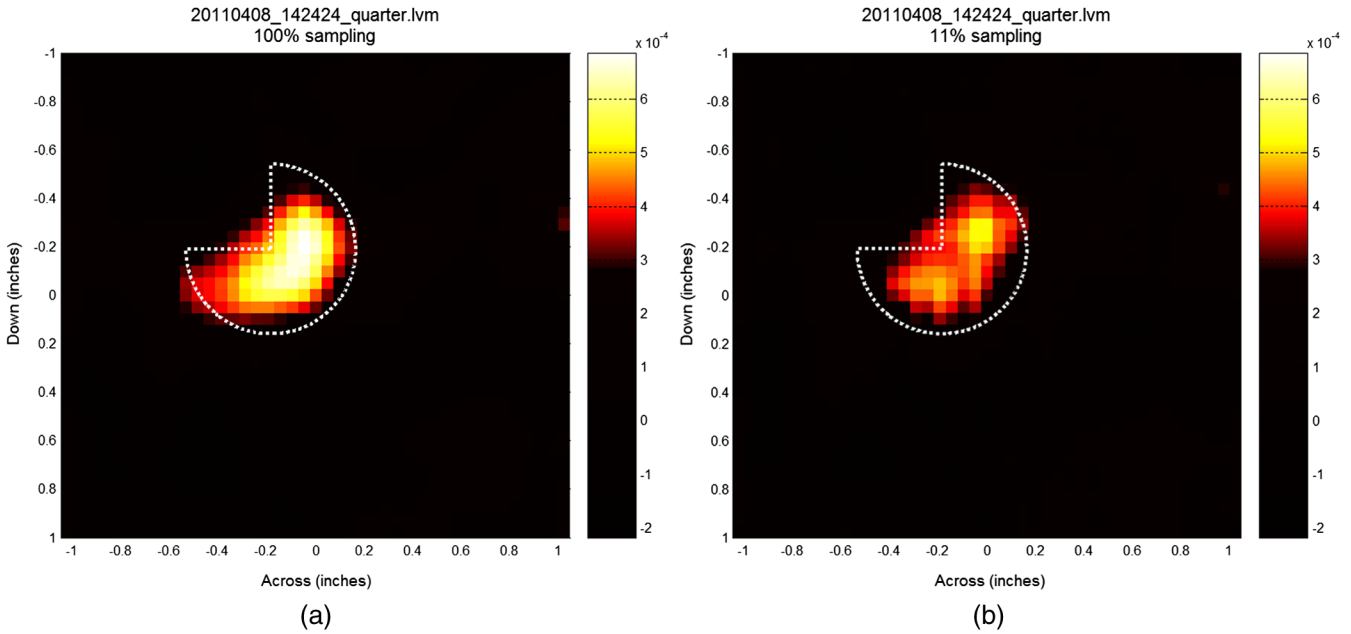

Fig. 13 Reconstructed image of lamp with one quarter of it blocked by a metal plate with (a) full and (b) 11% samples.

accurate image reconstruction with nonlinear minimization algorithms. The Hadamard patterns we employed for image acquisition would fit the CS framework if we had used, for example, a scrambled block Hadamard ensemble. While our imaging setup, in principle, can use such random acquisition matrices, we followed a slight variation of it in that the Hadamard patterns were chosen from a random selection of the rows of the *S*-matrix. The advantage we gained was the feasibility of real-time (relative to the integration time) image reconstruction as the reconstruction problem became linear, significantly reducing the computational complexity.

We used a Hadamard mask of 41×43 pixels, with pixel size of 1.24 mm, about half the wavelength of our 146 to 154 GHz radiometer. To introduce different Hadamard masks in the MMW beam path for compressive sensing, we designed an extended Hadamard mask of 81×85 pixels; a two-axis translational stage was used to expose different submasks of size 41×43 from the extended mask. Images were first reconstructed from a full set (1763) of Hadamard acquisitions. We devised an iterative relaxation method for image reconstruction from partial Hadamard acquisitions; the Hadamard space is efficiently extrapolated by a numerical relaxation procedure and the image reconstruction then uses standard (full set) inversion of the *S*-matrix. The reconstructed image of the object compared well in quality with the original image with as little as 11% of the full samples. We extended the relaxation method to implement a progressive sampling scheme in LabVIEW with near real-time reconstruction and image display. The image is reconstructed and displayed after each Hadamard acquisition; the acquisitions may continue until satisfactory image quality is obtained. Most test cases resulted in good-quality images with about 10 percent of the acquisitions, thus offering a factor-of-ten increase in imaging speed by adapting the CS approach.

Acknowledgments

This work is supported by the Office of Nonproliferation and Verification Research and Development under the National Nuclear Security Administration (NNSA) of the U.S. Department of Energy under Contract No. DE-AC02-06CH11357. The work of L. Spinoulas and A. K. Katsaggelos has been supported in part by a grant from the Department of Energy (DE-NA0000457).

References

1. C. Elachi, *Introduction to the Physics and Techniques of Remote Sensing*, Wiley, New York (1987).
2. M. P. Cadeddu and D. D. Turner, "Evaluation of water permittivity models from ground based observations of cold clouds at frequencies between 23 and 170 GHz," *IEEE Trans. Geosci. Remote Sens.* **49**(8), 2999–3008 (2011).
3. L. Yujiri, M. Shoucri, and P. Moffa, "Passive millimeter-wave imaging," *IEEE Microw. Mag.* **4**(3), 39–50 (2003).
4. R. Appleby and R. N. Anderton, "Millimeter-wave and submillimeter-wave imaging for security and surveillance," *Proc. IEEE* **95**(8), 1683–1690 (2007).
5. A. H. Lettington et al., "Passive millimeter-wave imaging architectures," *J. Optics A Pure Appl. Opt.* **5**(4), S103–S110 (2003).
6. M. R. Fetterman et al., "Simulation, acquisition, and analysis of passive millimeter-wave images in remote sensing applications," *Opt. Express* **16**(25), 20503–20515 (2008).
7. C. H. Townes and A. L. Schawlow, *Microwave Spectroscopy*, Dover, New York (1975).
8. N. Gopalsami et al., "Application of millimeter-wave radiometry for remote chemical detection," *IEEE Trans. Microw. Theory Tech.* **56**(3), 700–709 (2008).
9. N. Gopalsami et al., "Passive millimeter wave imaging and spectroscopy system for terrestrial remote sensing," *Proc. SPIE* **7670**, 767003 (2010).
10. S. Liao et al., "An efficient iterative algorithm for computation of scattering from dielectric objects," *Opt. Express* **19**(4), 3304–3315 (2011).
11. D. L. Donoho, "Compressed sensing," *IEEE Trans. Inf. Theory* **52**(4), 1289–1306 (2006).
12. M. Duarte et al., "Single-pixel imaging via compressive sampling," *IEEE Signal Process. Mag.* **25**(2), 83–91 (2008).
13. E. J. Candès, J. Romberg, and T. Tao, "Robust uncertainty principles: exact signal reconstruction from highly incomplete frequency information," *IEEE Trans. Inf. Theory* **52**(2), 489–509 (2006).
14. R. M. Willett, R. F. Marcia, and J. M. Nichols, "Compressed sensing for practical optical imaging systems: a tutorial," *Opt. Eng.* **50**(7), 072601 (2011).
15. W. L. Chan et al., "A single-pixel terahertz imaging system based on compressive sensing," *Appl. Phys. Lett.* **93**(12), 121105 (2008).
16. L. Gan, T. T. Do, and T. D. Tran, "Fast compressive imaging using scrambled block Hadamard ensemble," in *Proc. European Signal Processing Conference*, Lausanne, Switzerland (August 2008).
17. M. Harwit and N. Sloane, *Hadamard Transform Optics*, Academic Press, New York (1979).

18. J. Lynch, R. Matic, and J. Baron, "Performance limitations of compressive sensing for millimeter wave imaging," *Proc. SPIE* **7670**, 76700D (2010).
19. N. Gopalsami et al., "Compressive sampling in passive millimeter wave imaging," *Proc. SPIE* **8022**, 80220I (2011).
20. D. Jackson, *Classical Electrodynamics*, Wiley, New York (1998).
21. D. Babacan et al., "Compressive passive millimeter wave imaging," in *Proc. IEEE Int. Conf. in Image Processing (ICIP)*, Brussels, Belgium (2011).

Nachappa Gopalsami received his BE and MS degrees in electrical engineering from the University of Madras, India and PhD degree in electrical engineering and computer science from the University of Illinois, Chicago. He joined Argonne National Laboratory in 1980 where he is currently a senior electrical engineer in the sensors and instrumentation section of the nuclear engineering division. His current research interests include development of radio frequency, microwave, millimeter-wave, and terahertz sensors and imaging systems for national security, biosensing, environmental monitoring, and materials applications.

Shaolin Liao received a BS degree in materials science and engineering from Tsinghua University, Beijing, China, in July 2000, he received an MS degree in material science and an MS degree in electrical and computer engineering, both from the University of Wisconsin at Madison, in August 2003 and December 2005, respectively, and a PhD degree in electrical and computer engineering from the University of Wisconsin at Madison, in May 2008. He has held the research fellow position in the physics department, Queens College, City University of New York from May 2008 to January 2010. He is now with Argonne National Laboratory, doing microwave/millimeter wave/THz wave/laser research.

Thomas W. Elmer received a BS degree in physics with minors in math and computer science from La Sierra University in 1998 and an MS degree in physics from the University of Illinois, Chicago in 2004. While at La Sierra, he worked for the physics department, writing and maintaining programs to run laboratory experiments. He has also lectured on astronomy and gravitational physics for the department. In 1999 he joined Argonne National Laboratory as a student intern, eventually staying as a software engineering associate for the system technologies & diagnostics department of the nuclear engineering division. He writes programming for modeling, motion control, data acquisition, and data analysis in the microwave, millimeter-wave, and terahertz sensors labs.

Eugene R. Koehl received a BA in physics from Lewis University in 1969 and a BS in electrical engineering from Midwest College of Engineering (Illinois Institute of Technology) in 1981. He is an electrical engineer at Argonne National Laboratory with 37 years of experience in the design, fabrication, instrumentation, control, and automated data acquisition of experiments and facilities for testing the design and characteristics of sensors, power systems, and LMR components.

Alexander Heifetz is an electrical engineer in the nuclear engineering division at Argonne National Laboratory. Heifetz came to Argonne as a director's postdoctoral fellow in the nuclear engineering division. His research interests are in simulations and modeling for electromagnetic engineering, nuclear engineering, signal processing, and controls. He received a PhD in electrical engineering, MS in physics and BS (summa cum laude) in applied mathematics, all from Northwestern University. Heifetz has published over 20 peer-reviewed papers in major scientific journals, and has one provisional U.S. patent.

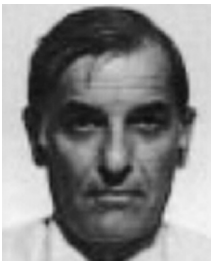

Apostolos C. Raptis is a senior electrical engineer at Argonne National Laboratory with 35 years of experience in teaching and in research and development. His areas of expertise include sensors, instrumentation and controls, nondestructive evaluation, data processing, electromagnetics, plasmas, optics, acoustics, and geophysical exploration. He is presently the department manager for systems technologies and diagnostics in the nuclear engineering division. At ANL he initiated and helped develop ANL's instrumentation and NDE (I&NDE) programs for nuclear and fossil energy, conservation, and arms controls. He is responsible for work on national security for remote detection of chemical, biological, nuclear agents, and explosives.

Leonidas Spinoulas received the BS degree in electrical and computer engineering from the National Technical University of Athens, Athens, Greece in 2010 and his MS degree in electrical engineering and computer science from Northwestern University, Evanston, IL, USA in 2012. He is currently pursuing a PhD degree in the department of electrical engineering and computer science of Northwestern University, Evanston, IL, USA.

Aggelos K. Katsaggelos received a diploma degree in electrical and mechanical engineering from the Aristotelian University of Thessaloniki, Greece, in 1979, and MS and PhD degrees in electrical engineering from the Georgia Institute of Technology, in 1981 and 1985, respectively. In 1985, he joined the department of electrical engineering and computer science at Northwestern University, where he is currently a professor holder of the AT&T chair. He is the co-author of Rate-Distortion Based Video Compression (Kluwer, 1997), Super-Resolution for Images and Video (Claypool, 2007), and Joint Source-Channel Video Transmission (Claypool, 2007).